Contents lists available at ScienceDirect

Materials Chemistry and Physics

journal homepage: www.elsevier.com/locate/matchemphys

Fine-grained magnetoelectric $Sr_{0.5}Ba_{0.5}Nb_2O_6$–$CoFe_2O_4$ composites synthesized by a straightforward one-pot method

Roberto Köferstein [*], Florian Oehler, Stefan G. Ebbinghaus

Institute of Chemistry, Martin Luther University Halle-Wittenberg, Kurt-Mothes-Straße 2, 06120, Halle, Germany

HIGHLIGHTS

- Straightforward synthesis for 0–3 $Sr_{0.5}Ba_{0.5}Nb_2O_6$–$CoFe_2O_4$ composites.
- Monitoring the phase evolution during sintering to ceramics bodies.
- Determination of Curie temperature.
- Impedance spectroscopy up to 200 °C and 10 MHz.
- Investigations of the magnetoelectric coefficient in dependence on magnetic DC field, frequency, and temperature.

GRAPHICAL ABSTRACT
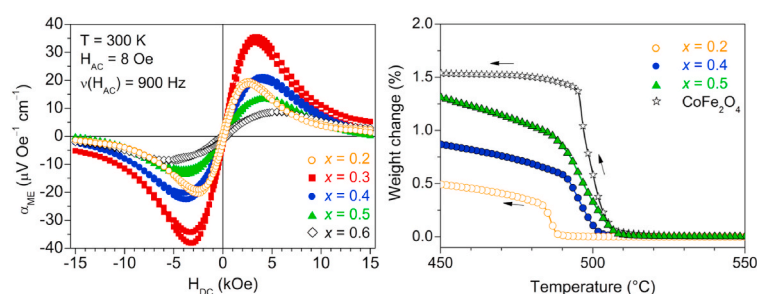
ARTICLE INFO

ABSTRACT

Magnetoelectric $(Sr_{0.5}Ba_{0.5}Nb_2O_6)_{1-x}$–$(CoFe_2O_4)_x$ (x = 0.2–0.6) composites were prepared by a one-pot soft-chemistry synthesis using PEG400. Calcining at 700 °C resulted in nanocrystalline composite powders ($d_{cryst.}$ = 24–30 nm) which were sintered between 1050 and 1200 °C to ceramic bodies with relative densities up to 98%. SEM investigations confirm the formation of composite ceramics with a 0–3 connectivity and variable grain sizes from 0.2 to 3.6 μm for sintering up to 1150 °C, while sintering at 1200 °C leads both to a change in the microstructure and a considerable grain growth. Magnetic measurements at 300 K reveal ferrimagnetic behaviour with saturation magnetization values smaller than bulk $CoFe_2O_4$ and coercivities between 790 and 160 Oe. Temperature-dependent impedance spectroscopy showed that the relative permittivities decrease both with rising frequency and $CoFe_2O_4$ fraction. The frequency dependence of the impedance can be well described using a single RC circuit. Magnetoelectric measurements show the presence of pronounced field hystereses. The maximum magnetoelectric coefficient (α_{ME}) depends both on the $CoFe_2O_4$ fraction (x) and sintering temperature. The composite with x = 0.3 exhibits the largest α_{ME} value of 37 μV Oe^{-1} cm^{-1} (@ 900 Hz). With rising frequency of the AC driving field α_{ME} increases up to 300–400 Hz and is nearly constant until 1 kHz.

1. Introduction

Multiferroics, i.e. materials, which exhibit at least two ferroic orders (e.g. ferromagnetism, ferroelectricity, and ferroelasticity) are of special interest because of their potential applications as e.g. memories, actuators, spintronics, and sensors [1,2], because the coupling of order parameters results in new functionalities. In particular, the coupling of ferro-/ferrimagnetic and ferroelectric phases leads to the so-called

---

magnetoelectric (ME) effect. The ME effect, first experimentally verified by Astrov in 1960 [3], allows to change the electrical polarization by applying a magnetic field (direct ME effect), or the magnetization by an electric field (converse ME effect). Single-phase ME materials like Cr_2O_3, $BiFeO_3$, or $BiMnO_3$ often show a rather small ME effect and/or it appears only at low temperatures [4–6]. In contrast, multiferroic composites, consisting of a ferroelectric and a ferrimagnetic compound show strong ME effects at room temperatures which is mandatory for practical applications [7]. In such composite materials the coupling between the ferroic phases is mediated through the interface. Magnetoelectric composites can be assembled in various connectivities such as 0–3, 2-2, 1–3, and 3-3 geometries, in which the numbers reflect the dimension in which each phase is self-connected [8]. Composites based on e.g. $BaTiO_3$ or $PbTiO_3$ as ferroelectric phase and ferrites as ferrimagnetic one have been extensively investigated [9–15]. In contrast, magnetoelectric composites containing $Sr_{0.5}Ba_{0.5}Nb_2O_6$ (SBN) are by far less well examined [16–26]. $Sr_xBa_{1-x}Nb_2O_6$ ($0.25 \leq x \leq 0.75$) is a lead-free relaxor ferroelectric with useful piezoelectric properties and crystallizes in the open tungsten-bronze structure [27–31]. The Curie temperature strongly depends on the Sr/Ba ratio and is about 120 °C for the composition $Sr_{0.5}Ba_{0.5}Nb_2O_6$ [28]. To prepare $Sr_{0.5}Ba_{0.5}Nb_2O_6-MFe_2O_4$ composites mainly the conventional mixed oxide method has been used [16–25], whereas Hoyos et al. [26] synthesized $Sr_{0.61}Ba_{0.39}Nb_2O_6-NiFe_2O_4$ composites by a Pechini-like soft-chemistry route. Usually, soft-chemistry routes, e.g. one-pot syntheses, lead to fine-grained powders which enable lower sintering temperatures resulting in ceramic bodies with tunable grain sizes [32,33].

In this paper, we describe a straightforward one-pot soft-chemistry synthesis route using PEG400 to synthesize $Sr_{0.5}Ba_{0.5}Nb_2O_6-CoFe_2O_4$ composites with a 0–3 connectivity and with different $CoFe_2O_4$ molar fractions. The first step of the synthesis leads to nanoscaled powders, which are sintered to fine-grained composite ceramics. Phase formation during calcination and sintering were monitored by XRD. Measurements of the magnetoelectric coupling were carried out depending on the magnetic DC field, frequency of the superimposed AC driving field, and temperature. Furthermore, the composite samples were characterized by magnetic measurements, impedance spectroscopy, and SEM.

2. Experimental

2.1. Material preparation

$(Sr_{0.5}Ba_{0.5}Nb_2O_6)_{1-x}-(CoFe_2O_4)_x$ (x = molar fraction) composites with x = 0.2, 0.3, 0.4, 0.5, and 0.6 were synthesized according to a polymerization method as described elsewhere [28].

For each composition 0.01 mol $NbCl_5$ (Alfa Aesar, 99%) was dissolved in 15 ml 2-methoxyethanol. Afterwards, 30 ml polyethylene glycol (PEG400) and 26 g citric acid were added and the mixture was stirred on a heating plate at 150 °C until it became a clear solution. $SrCl_2 \cdot 6H_2O$ (Merck, $\geq$ 99%) and $BaCl_2 \cdot 2H_2O$ (Fluka, $\geq$ 99%) (0.0025 mol each) were dissolved together in 7 ml 1,2-ethanediol and added to the hot Nb-solution. The resulting solution was stirred on the heating plate at 180 °C until it turned into a white suspension. According to the desired composition, stoichiometric amounts of $Co(NO_3)\cdot 6H_2O$ (Sigma-Aldrich, ACS) and $Fe(NO_3)\cdot 9H_2O$ (Merck, ACS) (n_{Co}/n_{Fe} = 1/2) were dissolved together in 5–10 ml 1,2-ethanediol and added to the (Sr,Ba, Nb)-suspension. The resulting brown reaction mixture was further stirred on the heating plate at 180 °C for about 3 h until it turned into a green, highly viscous suspension. The resulting (Sr,Ba,Nb,Co,Fe)-mixtures were calcined at 700 °C for 2 h (heating rate 10 K min^{-1}) in a muffle furnace in static air leading to $(Sr_{0.5}Ba_{0.5}Nb_2O_6)_{1-x}-(CoFe_2O_4)_x$ nano-powders. Ceramic bodies were obtained from these powders after mixing with 10 wt% of a saturated aqueous polyvinyl alcohol (PVA) solution as pressing aid and uniaxial pressing into pellets at about 85 MPa (green density: 2.2 g cm^{-3}). These pellets were placed on a ZrO_2 fibre mat and sintered to ceramic bodies between 1050 and 1200 °C

(heating-/cooling rate 5 K min^{-1}) with a soaking time of 1 h.

The chemical compositions of the composite powders, checked by XRF, agreed well with the expected values (Tab. S1, supporting information). In all samples, we found traces of 0.12–0.16 wt% CaO, which stem mainly from the strontium source.

For comparative purposes, pure $CoFe_2O_4$ was also prepared according to the described synthesis route.

2.2. Characterization

X-ray powder diffraction patterns were recorded at room temperature on a Bruker D8-Advance diffractometer, equipped with a one-dimensional silicon strip detector (LynxEye™) using Cu-K$_\alpha$ radiation and a counting time of 1 s per data point. Crystallite sizes and strain parameters were calculated from the XRD line broadening (integral peak breadth) using the software suite WinXPOW [34] applying the Scherrer and Wilson equations. Thermal analyses were performed with a heating-/cooling rate of 10 K min^{-1} in flowing nitrogen (75 ml min^{-1}) using a TA Instruments TGA 550 (weighing precision 0.01%). To determine the magnet transition temperature of $CoFe_2O_4$, a bar magnet was placed underneath the balance [35]. The specific surface area (BET) was determined by nitrogen five-point gasphysisorption (Nova touch 2LX, Quantachrome Corporation). The equivalent BET particle diameter was calculated assuming a spherical or cubic particle shape. XRF measurements were carried out with a Malvern Panalytical Epsilon 4. Scanning electron microscope images were recorded with a Phenom ProX SEM in the backscattered electron mode (BSE). Magnetic and magnetoelectric measurements were carried out using a Quantum Design PPMS9. Magnetic hysteresis loops were taken at 300 K with magnetic DC field cycling between −90 and +90 kOe. The samples were enclosed in gel capsules whose very small diamagnetic contribution was subtracted before data evaluation. For magnetoelectric and impedance investigations, ceramic bodies with a thickness of 1.2–1.4 mm were sputtered on both sides with 100 nm thick gold electrodes using a Cressington Sputter Coater 108auto. The samples for magnetoelectric measurements were electrically poled for 18 h at room temperature applying an electric field of about 6 kV cm^{-1} with a current limit of 0.1 mA [36]. Afterwards, the poled samples were short-circuited for 5 min. The magnetoelectric measurements were performed using a self-made setup [37] with the magnetic DC field parallel to the electrical polarization and a small AC driving field of about 8 Oe was superimposed collinear to the static field by a solenoid. The in-phase voltage (U_{ME}) was recorded using a lock-in technique. The magnetoelectric coefficient (α_{ME}) was calculated as α_{ME} = $U_{ME} \cdot (H_{AC} \cdot d)^{-1}$ with d being the sample thickness. The magnetoelectric behavior was investigated at 300 K using a DC field cycling between ± 15 kOe and $\nu(H_{AC})$ = 900 Hz. The dependence of the magnetoelectric coefficient on the AC field was measured between 20 and 1000 Hz. The temperature dependence of α_{ME} was measured between 50 and 300 K at $\nu(H_{AC})$ = 900 Hz. Both the frequency- and temperature-dependent measurements were done at the DC field at which the maximum of α_{ME} was found. An Impedance Analyzer 4192A (Hewlett Packard) was used for frequency- and temperature-dependent impedance measurements in ranges of 25–220 °C and 5 Hz − 10 MHz applying a voltage of 1 V.

3. Results and discussion

3.1. Synthesis and powder characterization

$(Sr_{0.5}Ba_{0.5}Nb_2O_6)_{1-x}-(CoFe_2O_4)_x$ composites with x = 0.2, 0.3, 0.4, 0.5, and 0.6, which corresponds to a $CoFe_2O_4$ weight fraction between 13.0 and 47.1%, were successfully prepared by the one-pot synthesis as described above. To obtain brown nanoscaled composite powders, the green viscous (Sr,Ba,Nb,Co,Fe)-solutions were calcined at 700 °C in a muffle furnace in static air (heating rate 5 K min^{-1}, soaking time 2 h). The XRD patterns (Fig. 1) of all samples show reflections corresponding
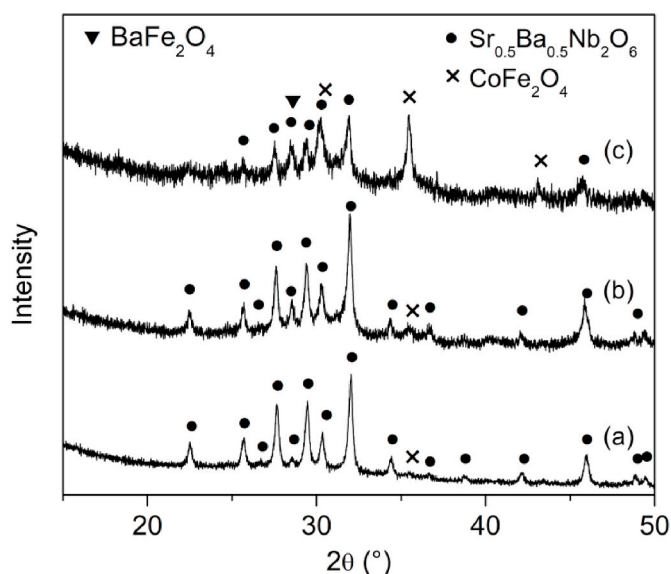
Fig. 1. Room-temperature XRD patterns of selected $(Sr_{0.5}Ba_{0.5}Nb_2O_6)_{1-x}-(CoFe_2O_4)_x$ composite powders after calcining at 700 °C for 2 h (heating rate 10 K min^{-1}): a) $x = 0.2$, b) $x = 0.4$, c) $x = 0.6$.

to tetragonal $Sr_{0.5}Ba_{0.5}Nb_2O_6$ (JCPDS #01-074-6520). XRDs for $x = 0.2$, 0.3, and 0.4 show only a weak reflection of cubic $CoFe_2O_4$ (JCPDS #00-022-1086), whereas for $x = 0.5$ and 0.6 the formation of crystalline $CoFe_2O_4$ can be clearly seen. Additionally, an increasing peak intensity at $2\theta \approx 28.5°$ for composite powders with $x = 0.5$ and 0.6 points to the formation of orthorhombic $BaFe_2O_4$ (JCPDS #00-025-1191) as an intermediate phase, which disappears after calcining at 800 °C (Fig. S1, supporting information). A slightly increasing background level primarily between $2\theta = 20–30°$ suggests an amorphous fraction in all samples.

The specific surface areas of the $(Sr_{0.5}Ba_{0.5}Nb_2O_6)_{1-x}-(CoFe_2O_4)_x$ powders, derived from BET measurements, decrease with increasing $CoFe_2O_4$ content from 31(3) to 21(2) m^2 g^{-1} corresponding to equivalent primary particle sizes of 36(3) and 53(2) nm for $x = 0.2$ and $x = 0.6$, respectively (see Fig. 2). The volume-weighted average crystallite size
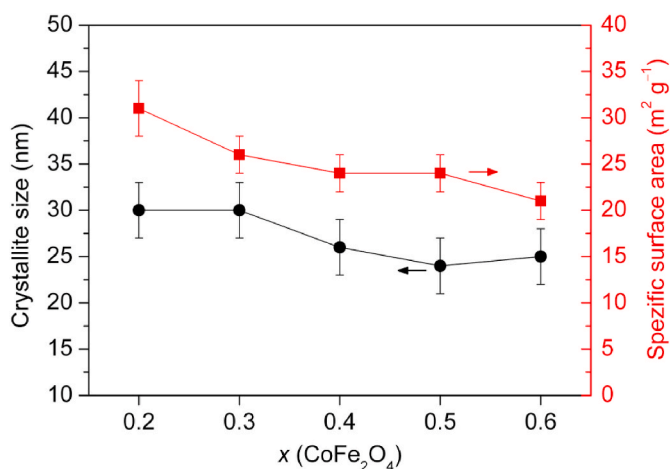
(size of a coherent scattering domain) obtained from the XRD peaks of the $Sr_{0.5}Ba_{0.5}Nb_2O_6$ phase is between 30(3) and 24(3) nm. The difference between the crystallite size and the primary particle size is most likely caused by the formation of closely joined crystallites with surface areas unavailable for nitrogen adsorption [38]. Furthermore, each primary particle may consist of more than one crystallite domain.

3.2. Sintering, microstructure, and phase composition of ceramic bodies

After pressing the nanocrystalline composite powders into pellets and sintering at temperatures between 1050 and 1200 °C for 1 h (heating-/cooling rate: 5 K min^{-1}) black-brown ceramic bodies were obtained. Their bulk densities were calculated from the weight and geometric dimension and related to the single crystal densities of $Sr_{0.5}Ba_{0.5}Nb_2O_6$ and $CoFe_2O_4$ considering their nominal molar fractions [39]. As shown in Fig. 3, the densities increase between 1050 and 1150 °C. Dense ceramic bodies (relative density ≥90%) were obtained after sintering above 1075 °C. Firing up to 1150 °C leads to ceramic bodies with relative densities of 98(1) %. Upon further increasing the sintering temperature to 1200 °C the densities of most samples did not change, however, for $x = 0.5$ and 0.6 the densities slightly decreased to 92(1) % due to the change in the microstructure as described below.

Representative microstructures of the surface of the composite ceramics are shown in Fig. 4. In the applied BSE mode, the dark grains correspond to $CoFe_2O_4$ while the light grey ones are $Sr_{0.5}Ba_{0.5}Nb_2O_6$. Upon sintering at 1150 °C the $Sr_{0.5}Ba_{0.5}Nb_2O_6$ phase forms globular- or irregular-shaped particles, while the $CoFe_2O_4$ phase consists of pyramidal- and octahedral-like grains as shown in Fig. 4a and b for $x = 0.3$ and 0.6, respectively. Sintering at 1200 °C leads to a change of the microstructure as can be seen in Fig. 4c and d. At this temperature $Sr_{0.5}Ba_{0.5}Nb_2O_6$ (SBN) forms predominantly small pillars besides some globular-like grains. The fraction of the globular-like grains of SBN decreases with increasing $CoFe_2O_4$ fraction (x) which is most-likely the reason for reduced bulk densities at $x = 0.5$ and 0.6. Similar observations were done in pure SBN ceramics [28]. The $CoFe_2O_4$ (CFO) particles retain their octahedron-/pyramidal-like shape. The grain diameters range between about 0.2 and 1.3 μm (SBN) and 0.3–1.1 μm (CFO) after sintering at 1075 °C and increase to 0.3–1.6 μm (SBN)/0.6–2.6 μm (CFO) and 0.5–3.6 μm (SBN)/0.6–3.4 μm (CFO) after 1100 °C and 1150 °C,

Fig. 2. Development of the crystallite size of $Sr_{0.5}Ba_{0.5}Nb_2O_6$ and specific surface area depending on the fraction of $CoFe_2O_4$ of $(Sr_{0.5}Ba_{0.5}Nb_2O_6)_{1-x}-(CoFe_2O_4)_x$ composite powders calcined at 700 °C for 2 h (heating rate 10 K min^{-1}).
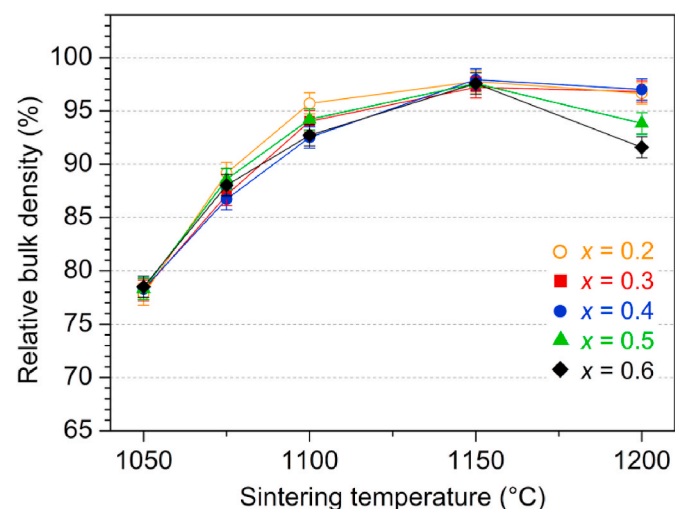
Fig. 3. Relative bulk densities of $(Sr_{0.5}Ba_{0.5}Nb_2O_6)_{1-x}-(CoFe_2O_4)_x$ composite ceramic bodies versus sintering temperatures (soaking time 1 h, heating rate 5 K min^{-1}).

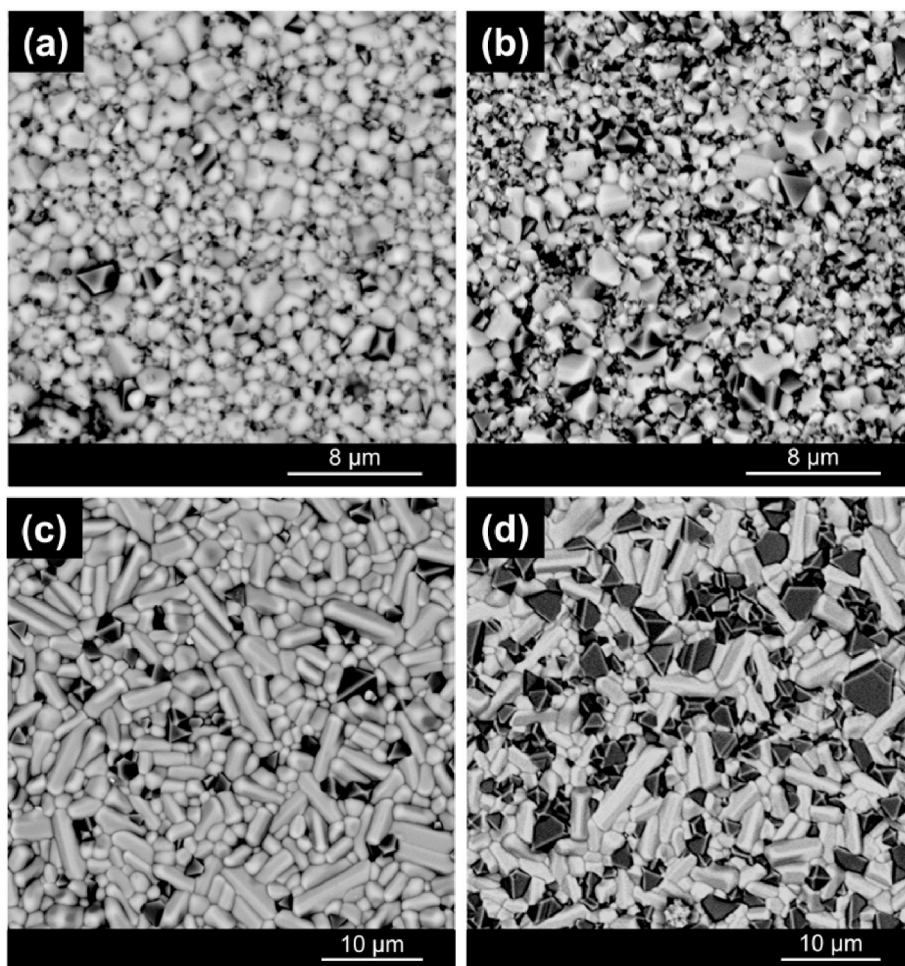**Fig. 4.** SEM-BSE images of selected $(Sr_{0.5}Ba_{0.5}Nb_2O_6)_{1-x}-(CoFe_2O_4)_x$ composite ceramics sintered at different temperatures (T_s) for 1 h. (a) $x = 0.3$, $T_s = 1150\ °C$, (b) $x = 0.6$, $T_s = 1150\ °C$, (c) $x = 0.3$, $T_s = 1200\ °C$, (d) $x = 0.6$, $T_s = 1200\ °C$.

respectively. Firing at 1200 °C SBN forms pillars with lengths in the range of about 2–14 μm and widths between 1.5 and 3 μm corresponding to an aspect ratio between 2 and 6. Besides the pillars, the sizes of the globular-like grains are between 1 and 5 μm and the octahedral-like $CoFe_2O_4$ grains are between 1.5 and 6 μm. The grain sizes of all samples are listed in Tab. S2 (supporting information). The grain sizes of both components considerably rise with sintering temperature. With increasing $CoFe_2O_4$ fraction (x) we observed a tendency of increasing sizes of the $CoFe_2O_4$ grains while the SBN particles are not affected by x.

Powder XRD patterns of selected sintered composite ceramics are shown in Fig. 5. All patterns show strong and sharp reflections of the target phases $Sr_{0.5}Ba_{0.5}Nb_2O_6$ and $CoFe_2O_4$. Sintering between 1050 and 1150 °C leads to small amounts of monoclinic $FeNbO_4$ (JCPDS #01-071-1849) with a fraction of about 3–4 wt%. In contrast, after sintering at 1200 °C, the $FeNbO_4$ phase vanished, while the formation of 2–3 wt% tetragonal $CoNb_2O_6$ (JCPDS #01-075-2340) was observed. The appearance of secondary phases is caused by interdiffusion processes between $Sr_{0.5}Ba_{0.5}Nb_2O_6$ and $CoFe_2O_4$. The amounts of both secondary phases do not change significantly with the fraction of $CoFe_2O_4$. In contrast, a Pechini-like synthesis by Hoyos et al. [26] with 1,2-ethanediol at pH = 9 led to the formation of secondary phases up to 17 wt%. Thus, our synthesis route leads to composite ceramics with much higher purity.
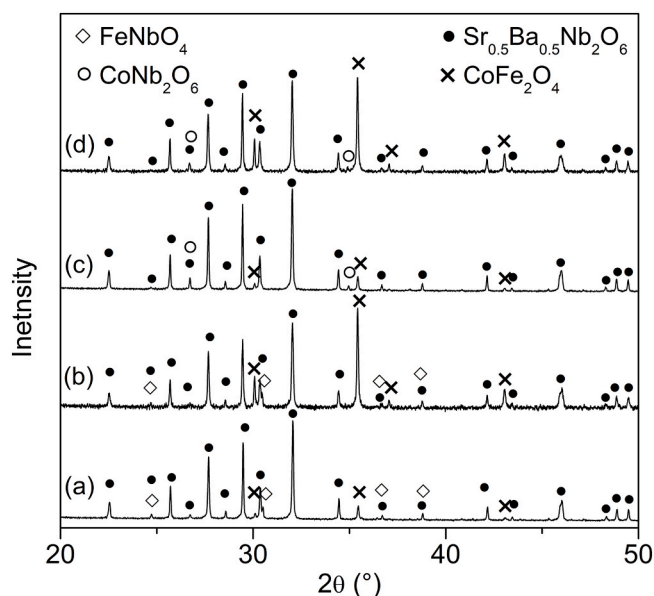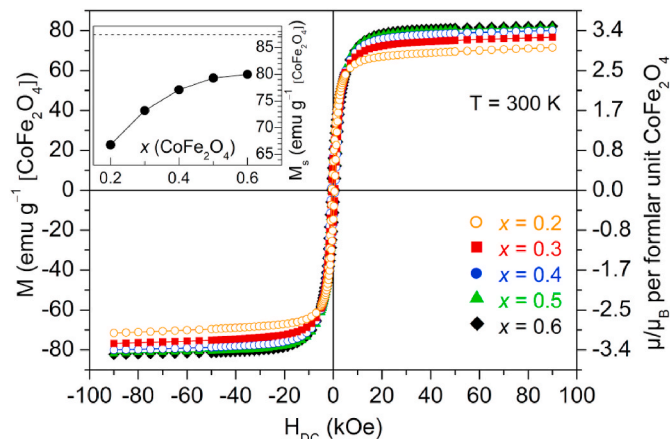

Fig. 5. Room-temperature powder XRD patterns of crushed $(Sr_{0.5}Ba_{0.5}Nb_2O_6)_{1-x}-(CoFe_2O_4)_x$ composite ceramics after sintering at different temperatures (T_s) for 1 h (heating-/cooling rate 5 K min^{-1}): a) $x = 0.2$, $T_s = 1150\ °C$, b) $x = 0.6$, $T_s = 1150\ °C$, c) $x = 0.2$, $T_s = 1200\ °C$, d) $x = 0.6$, $T_s = 1200\ °C$.

Fig. 6. Field dependence of the magnetization at 300 K for composite ceramics sintered at 1100 °C for 1 h. The inset shows the saturation magnetization (M_s) depending on the $CoFe_2O_4$ fraction (x). The horizontal line represents the value of M_s measured for pure $CoFe_2O_4$. The uncertainties of M_s (≤ 0.06 emu g^{-1}) are smaller than the symbol sizes. The magnetization is given with respect to the nominal $CoFe_2O_4$ mass.

3.3. Magnetic behavior

Fig. 6 exemplarily shows the field-dependent magnetization at 300 K of ceramics sintered at 1100 °C. Data have been normalized with respect to the $CoFe_2O_4$ fraction. All samples show hystereses due to the ferrimagnetic nature of $CoFe_2O_4$. The saturation magnetizations (M_s) for the composite samples were calculated by extrapolating the magnetization at high field to H = 0 because of the presence of small amounts of paramagnetic secondary phases ($FeNbO_4$, $CoNb_2O_6$), as aforementioned [40–43]. The M_s values of the $(Sr_{0.5}Ba_{0.5}Nb_2O_6)_{1-x}-(CoFe_2O_4)_x$ ceramics sintered at 1100 °C increase with rising $CoFe_2O_4$ content from 66.8(6) for $x = 0.2$ to 80.0(2) emu g^{-1} for $x = 0.6$ (inset in Fig. 6). The same trend was found for composite ceramics sintered at other temperatures (see Fig. S2, supporting information).

The difference between the calculated M_s values of the composites and the M_s value of 87.4(1) emu g^{-1} (3.67(1) μ_B f.u.$^{-1}$) of pure $CoFe_2O_4$ (sintered at 1100 °C) is most likely due to the formation of nonferro-/nonferrimagnetic $FeNbO_4$ and CoN_2O_6 secondary phases [41–43] and the observed grain growth of the $CoFe_2O_4$ grains with increasing x. Additionally, the shape of the grains may affect M_s. As mentioned above, the $CoFe_2O_4$ grains in the composites have a pyramidal-/octahedral-like shape, while the grains in the $CoFe_2O_4$ bulk ceramic consists of globular-like grains. Shen at al [44] observed in micro-sized $NiFe_2O_4$ with octahedral grains a reduced saturation magnetization compared to the bulk value. The decrease of M_s with decreasing $CoFe_2O_4$ content can be explained on basis of the mentioned impurities, because the fraction of these paramagnetic, secondary phases is nearly independent on the nominal $CoFe_2O_4$ content. Its relative effect is larger for lower values of x. The M_s values (Fig. 7) of the composites vary slightly with sintering temperature due to increasing $CoFe_2O_4$ grain sizes as demonstrated for the sample with $x = 0.3$ (inset I in Fig. 7). In contrast, the coercivities (H_c) strongly decrease with sintering temperature, because of grain growth of the ferrite phase [45–47], whereas the dependence on the $CoFe_2O_4$ content is marginal (inset II in Fig. 7).

To determine the paramagnetic ⇆ ferrimagnetic transition temperature T_C (Curie-temperature) of the $CoFe_2O_4$ phase in the composites we performed thermogravimetric measurements in which a magnet was attached under the furnace of the thermobalance. In the ferrimagnetic temperature region, the magnet applies an extra attractive force on the hanging sample, resulting in an apparent higher weight. Thus, during cooling down from 650 °C (paramagnetic state) the weight of the samples remains almost constant until T_C is reached, where a sudden
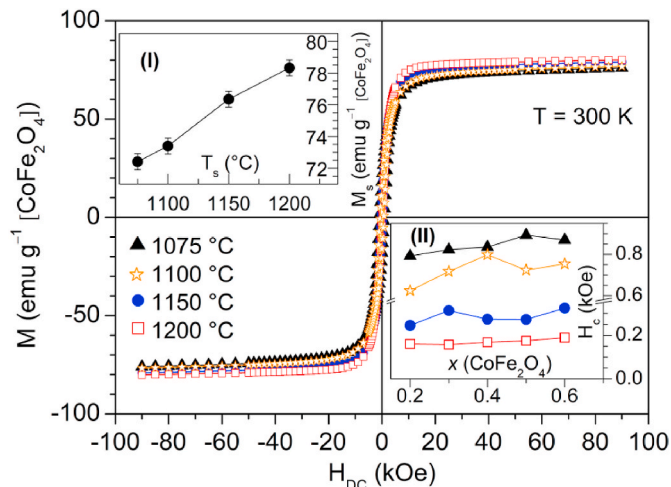

Fig. 7. Magnetization (M) versus applied field (H_{DC}) at 300 K of $(Sr_{0.5}Ba_{0.5}Nb_2O_6)_{0.7}-(CoFe_2O_4)_{0.3}$ composite bodies sintered at the indicated temperatures for 1 h. Inset (I) shows the saturation magnetization (M_s) depending on the sintering temperature (T_s). Inset (II) shows the coercivities as a function of the $CoFe_2O_4$ fraction (x) for different sintering temperatures. Uncertainties of the coercivities values (≤ 20 Oe) are smaller than the symbol sizes. The magnetization is given with respect to the nominal $CoFe_2O_4$ mass.
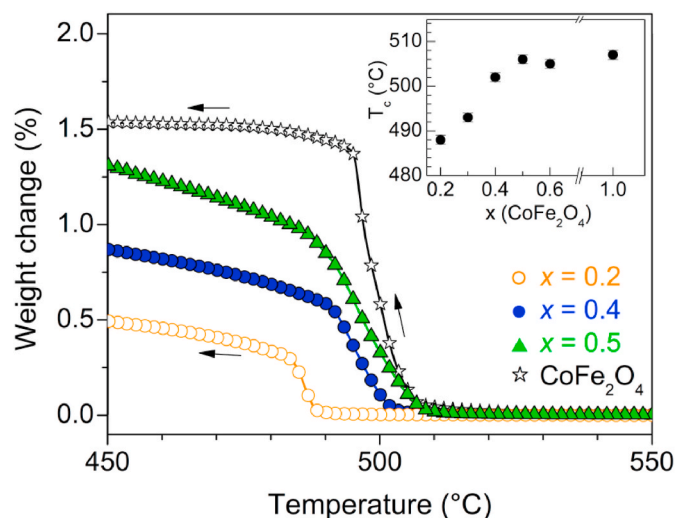

Fig. 8. Thermogravimetric investigations in flowing nitrogen (cooling rate 10 K min^{-1}) in a magnetic field for selected $(Sr_{0.5}Ba_{0.5}Nb_2O_6)_{1-x}-(CoFe_2O_4)_x$ and pure $CoFe_2O_4$ ceramic bodies sintered at 1100 °C for 1 h. For the sake of clarity, only every 20th data point is shown as a symbol. The inset shows T_c depending on the $CoFe_2O_4$ fraction (x).

increase in weight is observed. T_C was determined from the onset of the weight increase. As demonstrated for selected samples in Fig. 8, the Curie temperature increases slightly with increasing $CoFe_2O_4$ content and amount to 488(1), 493(1), 502(1), 506(1), and 505(1) °C for $x = 0.2, 0.3, 0.4, 0.5, 0,6$, respectively, while for pure $CoFe_2O_4$ ceramics T_C was determined as 507(1) °C. We suppose, the decrease of T_C at lower $CoFe_2O_4$ fraction is due to interdiffusion processes resulting in the formation of $CoFe_2O_4$ grain boundaries containing Sr/Ba/Nb-ions and/or vacancies [48,49]. Gashemi [48] found a reduced Curie temperature in Sr-doped $CoFe_2O_4$ with rising doping level. As mentioned above, related to the whole $CoFe_2O_4$ fraction the amount of such doped grain boundaries increases with decreasing ferrite content.
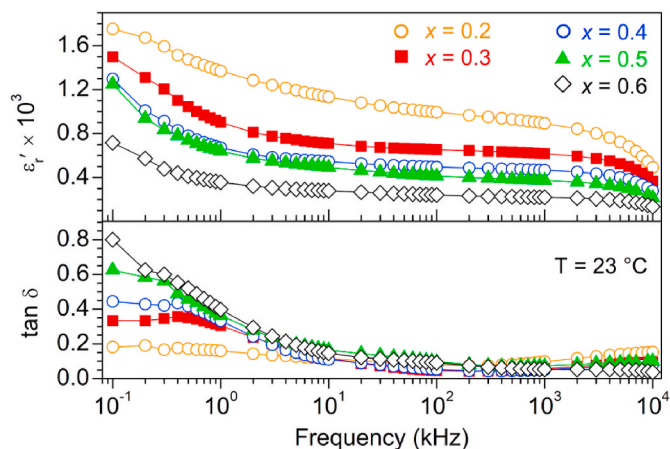
Fig. 9. Frequency dependence of the real part of the permittivity (ε_r') and tan δ at room temperature of $(Sr_{0.5}Ba_{0.5}Nb_2O_6)_{1-x}-(CoFe_2O_4)_x$ ceramic bodies sintered at 1100 °C.
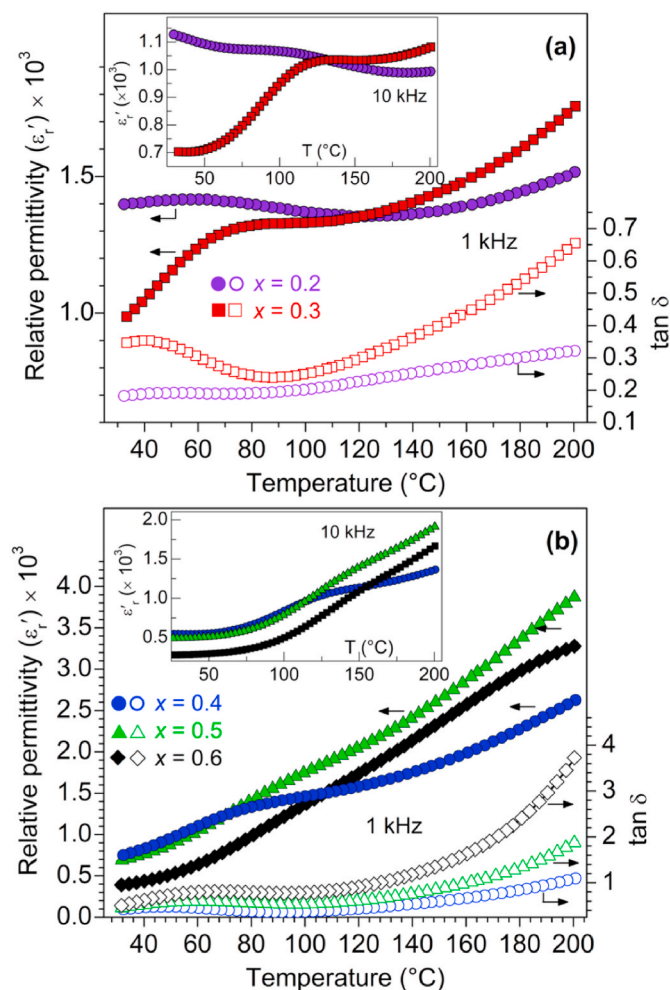
Fig. 10. Temperature dependence of the real part of the permittivity (ε_r', closed symbols) and tan δ (open symbols) at 1 kHz of $(Sr_{0.5}Ba_{0.5}Nb_2O_6)_{1-x}-(CoFe_2O_4)_x$ ceramic bodies sintered at 1100 °C. (a) $x = 0.2$ and 0.3, (b) $x = 0.4, 0.5, 0.6$. The insets show the temperature dependence of ε_r' at 10 kHz. For the sake of clarity only every third data point is represented by a symbol.

3.4. Impedance spectroscopy

Impedance spectroscopy was carried out on composite ceramics sintered at 1100 °C. The development of the real part of the relative permittivity (ε_r') and dissipation factor (tan δ) with the applied frequency at room temperature is shown in Fig. 9.

All composites show slightly decreasing permittivities and tan δ values with rising frequency, with a strong decrease of ε_r' above about 2 MHz. This behavior is most likely due to the Maxwell−Wagner interface polarization caused by electrically conductive particles ($CoFe_2O_4$) embedded in an insulating matrix ($Sr_{0.5}Ba_{0.5}Nb_2O_6$) [50,51]. Additionally, ε_r' becomes smaller with rising $CoFe_2O_4$ fraction which is typical for ferrite−ferroelectric composites [52–55]. Simultaneously, tan δ increases with rising $CoFe_2O_4$ content reflecting the electrically leaky nature of ferrites (see Fig. 9). In Fig. 10 the temperature dependence of ε_r' and tan δ at a frequency of 1 kHz are shown. The permittivity values of $(Sr_{0.5}Ba_{0.5}Nb_2O_6)_{0.8}-(CoFe_2O_4)_{0.2}$, which is the most insulating sample even at high temperatures, vary only slightly up to a temperature of 200 °C. The samples with $CoFe_2O_4$ contents of $x = 0.3$ and 0.4 show a broad shoulder roughly between 80 and 130 °C, whereas the permittivity values of composites with $x = 0.5$ and 0.6 increase continuously with temperature and reach values of 3300 and 3900 at 200 °C, respectively. Rising permittivity values at higher temperatures go along with an increase in the loss tangents, most likely due to an increasing conductivity of these samples. A clear ferroelectric ⇆ paraelectric phase transition maxima of the $Sr_{0.5}Ba_{0.5}Nb_2O_6$ phase could not be observed. However, at 1 kHz the samples with ferrite contents of $x = 0.2$, 0.3, and 0.4 show the formation of a weak shoulder below 130 °C, which may be attributed to the ferroelectric ⇆ paraelectric phase transition. The shoulder is more pronounced at higher frequencies (see insets in Fig. 10). In contrast, single $Sr_{0.5}Ba_{0.5}Nb_2O_6$ shows a clear phase transition at about 120 °C (see Fig. S3, supporting information) [28,56]. However, Chen et al. [17] and Lin et al. [18] found a broad phase transition temperature below 25 °C in $Sr_{0.5}Ba_{0.5}Nb_2O_6–CoFe_2O_4$ composites prepared by the conventional mixed-oxide method. We suppose that the considerable broadening of the phase transition maxima is caused by doping of $Sr_{0.5}Ba_{0.5}Nb_2O_6$ with Co^{2+} and/or Fe^{3+}. Kim et al. [57] and Kshirsagar et al. [58] observed a broadening of the phase transition in iron/cobalt-doped $Sr_{0.5}Ba_{0.5}Nb_2O_6$. Our findings are in accordance with investigations by Rathore and Vitta [25] on $Sr_{0.5}Ba_{0.5}Nb_2O_6$−ferrite composites who also observed a broadening and reduction of the phase transition temperature.

The conductivity of the $(Sr_{0.5}Ba_{0.5}Nb_2O_6)_{1-x}-(CoFe_2O_4)_x$ ceramics is rather low ($\sigma_{DC} \ll 10^{-7}$ S cm^{-1}) at room temperatures. While the ceramic with $x = 0.2$ remains insulating even at high temperatures, the composite ceramics with $x = 0.3–0.6$ exhibit considerable DC conductivities at elevated temperatures suggesting a semiconducting nature. Therefore, the high-temperature impedance data were modelled using an equivalent circuit consisting of one resistance-capacitor (RC) element including a constant phase shift element. The specific complex impedance (ρ^*) for a single RC element is described by:

$$\rho^* = \frac{\rho_{DC}}{1 + (i\omega\tau)^\beta} \tag{1}$$

where, β is the constant phase shift (CPE) coefficient and $\tau = \rho_{DC}\varepsilon\varepsilon_0$. Details of this approach have been reported elsewhere [59]. The resulting Cole-Cole plots (Fig. 11) reveal single semicircular arcs up to 220 °C, indicating that the impedance data can be well described by the applied model. Hence, bulk and grain boundary contributions on impedance cannot be distinguished, which may be the result of the high density and large grain sizes of our ceramics, reducing the effect of grain boundaries. The calculated DC resistivities (ρ_{DC}) decrease continuously with rising $CoFe_2O_4$ content, e.g. from $1.63(5)\cdot10^5$ kΩ cm ($x = 0.3$) to 83 (3) kΩ cm ($x = 0.6$) at 220 °C.
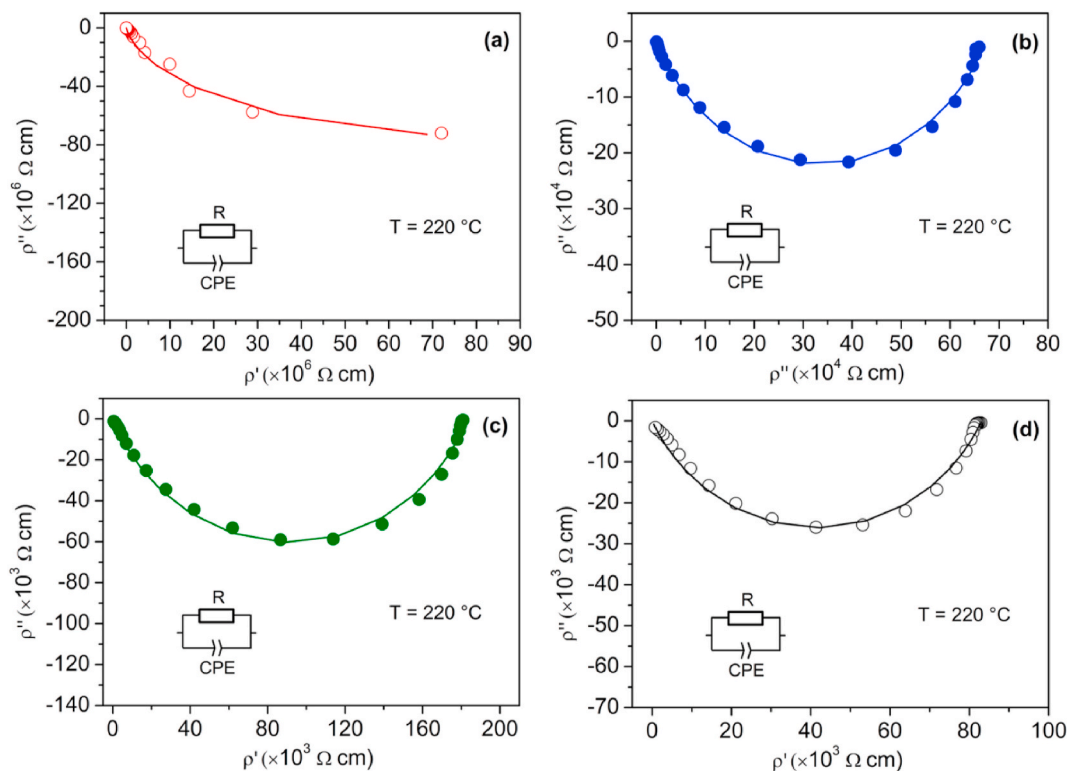
Fig. 11. Cole−Cole plots of $(Sr_{0.5}Ba_{0.5}Nb_2O_6)_{1-x}−(CoFe_2O_4)_x$ ceramics sintered at 1100 °C. a) $x = 0.3$, b) $x = 0.4$, c) $x = 0.5$, d) $x = 0.6$.

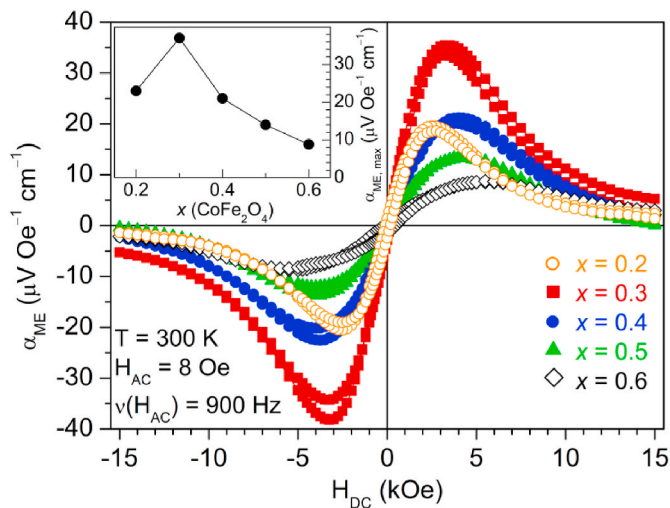**Fig. 12.** Magnetoelectric coefficient (α_{ME}) vs. magnetic DC field for various composite ceramics sintered at 1100 °C for 1 h. The inset shows the maximum magnetoelectric coefficient (α_{MEmax}) depending on the $CoFe_2O_4$ fraction (x). The uncertainty of the data (1 μV Oe^{-1} cm^{-1}) is smaller than the symbol size.

3.5. Magnetoelectric properties

Fig. 12 exhibits the dependence of the magnetoelectric coefficient (α_{ME}) at 300 K on the static magnetic field (H_{DC}) for composite ceramics sintered at 1100 °C. Composites sintered at other temperatures show analogous behaviors (Fig. S4 and S5, supporting information).

Starting from the maximum field of 15 kOe, α_{ME} increases with decreasing DC field up to a maximum (α_{MEmax}) and almost vanishes at zero field. For negative fields an inverse behavior is observed. Upon reversing sweep direction of the H_{DC} field small hystereses are found with coercivities up to 250 Oe. The magnetic DC field at which α_{ME}

reaches its maximum ($H_{\alpha max}$) increases with the $CoFe_2O_4$ fraction in the composites, e.g. for $x = 0.2$ the maximum for α_{ME} appears at 3.0 kOe, whereas for $x = 0.6$ the maximum α_{ME} value is found at 5.5 kOe (Fig. S6, supporting information). Also, the magnetoelectric coefficient depends on the $CoFe_2O_4$ content and shows a maximum of $\alpha_{ME} = 37(1)$ μV Oe^{-1} cm^{-1} ($\nu(H_{AC}) = 900$ Hz) at $x = 0.3$ while further increasing of the $CoFe_2O_4$ content leads to decreasing α_{ME} values (inset in Fig. 12). This behaviour is somewhat different from our results for $BaTiO_3–CoFe_2O_4$ or $BaTiO_3–Ni$ for which the maxima were found around $x = 0.4$ [36,37,60]. We assume that the decrease of α_{MEmax} with higher ferrite content is due to an increase of the conductivity leading to an inner discharging (see impedance section). The maximum α_{ME} value was further found to depend on the sintering temperature, e.g.
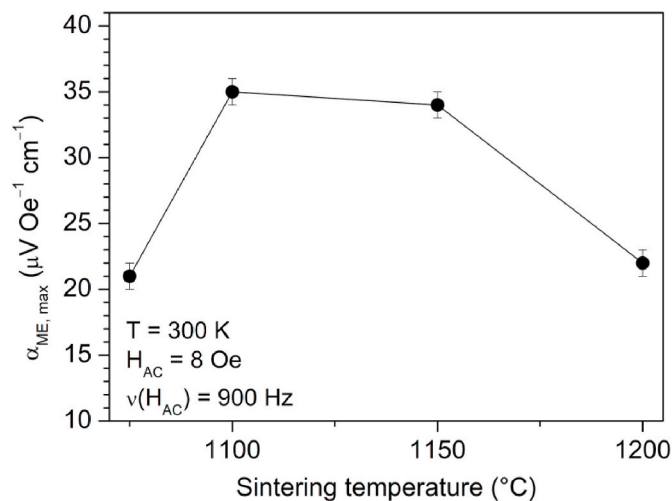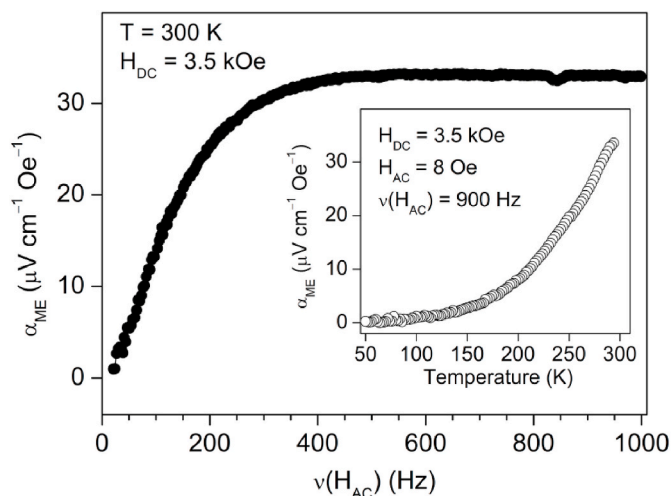

Fig. 13. Maximum magnetoelectric coefficient (α_{MEmax}) depending on the sintering temperature for $(Sr_{0.5}Ba_{0.5}Nb_2O_6)_{0.7}−(CoFe_2O_4)_{0.3}$ composite ceramics.

Fig. 14. Frequency dependence (H_{AC}) of α_{ME} for $(Sr_{0.5}Ba_{0.5}Nb_2O_6)_{0.7}-(CoFe_2O_4)_{0.3}$ sintered at 1100 °C for 1 h. The inset shows the temperature dependence of α_{ME}.

$(Sr_{0.5}Ba_{0.5}Nb_2O_6)_{0.8}-(CoFe_2O_4)_{0.2}$ shows its highest α_{ME} value after sintering at 1150 °C, whereas for composites with $x \geq 0.3$ the optimal sintering temperature is 1100 °C as demonstrated for $(Sr_{0.5}Ba_{0.5}Nb_2O_6)_{0.7}-(CoFe_2O_4)_{0.3}$ in Fig. 13. Decreasing α_{ME} values after sintering at 1200 °C get along with an increase of conductivity of at least one order of magnitude.

The evolution of α_{ME} at $H_{\alpha max}$ at 300 K with the frequency of the AC driving field is exemplarily shown for $x = 0.3$ in Fig. 14. For all composites we observe a strong increase of the magnetoelectric coefficient up to 300–400 Hz, while from about 400 Hz to 1000 Hz α_{ME} does not change significantly. The increase of α_{ME} at low frequencies can be explained by a partial internal discharge due to the conductivity of $CoFe_2O_4$ [61]. Furthermore, Bichurin and Petrov [62] showed that in 0–3 composites charge accumulation lead to an inverse Maxwell-Wagner-type relaxation leading to a charging of the capacitance which increases with frequency and saturates at higher frequencies. A similar behaviour was also found in $BaTiO_3-CoFe_2O_4$, $BaTiO_3-Ni$ and $Pb(Mg_{1/3}Nb_{2/3})-PbTiO_3-CoFe_2O_4$ composites [36,37, 60,63]. This finding is in contrast to the one of Sutar et al. [64] and Jigajeni et al. [65] who observed a continuous increase of α_{ME} up to about 5 kHz in ferrite−strontium barium niobate composites. As seen in the inset in Fig. 14 α_{ME} becomes continuously lower with decreasing temperature and below about 100 K the magnetoelectric coupling nearly vanishes. This temperature dependence of α_{ME} reflects the decreasing piezoelectric and ferroelectric character of strontium barium niobate with decreasing temperature [27,66–69] and supports the strain-mediated mechanism of the magnetoelectric effect as a tensor product property of the magnetostrictive ($CoFe_2O_4$) and the piezoelectric ($Sr_{0.5}Ba_{0.5}Nb_2O_6$) components [2,14,70]. A decreasing of the magnetoelectric coupling with declining temperature has also recently been observed in $BaTiO_3-CoFe_2O_4$ and $BaTiO_3-Ni$ composites [36,60]. For the latter system the low temperature phase transitions of $BaTiO_3$ could be detected in the ME signal. As $Sr_{0.5}Ba_{0.5}Nb_2O_6$ does not possess such transitions no anomalies were observed here.

4. Conclusion

Magnetoelectric $(Sr_{0.5}Ba_{0.5}Nb_2O_6)_{1-x}-(CoFe_2O_4)_x$ composites were synthesized by a one-pot polymerization method with PEG400. Calcining at 700 °C resulted in brown nanocrystalline composite powders with specific surface areas between 31(3) and 21(2) $m^2\ g^{-1}$ and crystallite sizes of 24(3) to 30(3) nm. Sintering of the nano-powders up to 1150 °C led to ceramic bodies with relative densities up to 98(1) %

and grain sizes between 0.2 and 3.6 μm. At 1200 °C the microstructure changed significantly with the formation of pillar-like $Sr_{0.5}Ba_{0.5}Nb_2O_6$ particles. XRD investigations showed the appearance of only small amounts (2–4 wt%) of secondary phases besides the main components $Sr_{0.5}Ba_{0.5}Nb_2O_6$ and $CoFe_2O_4$. The relative permittivities of the composites decrease with increasing $CoFe_2O_4$ content and frequency. Temperature-dependent measurements show increasing permittivities and tan δ values, the impedance of the samples can be described with a single RC-equivalent circuit and the DC conductivity increases with higher $CoFe_2O_4$ content. Field-dependent measurements of the magnetoelectric coupling show a hysteresis of the magnetoelectric coefficient (α_{ME}) with maxima/minima at DC magnetic fields between ±3.0 kOe and ±5.5 kOe depending on the $CoFe_2O_4$ fraction. The maximum magnetoelectric coefficient of 37(1) $\mu V\ Oe^{-1}\ cm^{-1}$ (@ 900 Hz) was found in $(Sr_{0.5}Ba_{0.5}Nb_2O_6)_{0.7}-(CoFe_2O_4)_{0.3}$ composites. For all samples, the magnetoelectric coefficient decreases at lower temperatures. Furthermore, the variation of the H_{AC} frequency results in almost constant α_{ME} values between 400 and 1000 Hz, while below 400 Hz α_{ME} becomes continuously smaller. The facile synthesis described in this article leads to the formation of magnetoelectric composite ceramics with only minor traces of secondary phases and a fine-grained microstructure compared to the conventional mixed oxide synthesis. The microstructure and thus the magnetoelectric coefficient may be tuned using sintering additives which is a subject of further investigations.

CRediT authorship contribution statement

Roberto Köferstein: Conceptualization, Data curation, Formal analysis, Investigation, Project administration, Resources, Validation, Visualization, Writing – original draft, Writing – review & editing. **Florian Oehler:** Data curation, Formal analysis, Writing – original draft. **Stefan G. Ebbinghaus:** Conceptualization, Project administration, Resources, Supervision, Validation, Writing – original draft, Funding acquisition.

Declaration of competing interest

The authors declare that they have no known competing financial interests or personal relationships that could have appeared to influence the work reported in this paper.

Appendix A. Supplementary data

Supplementary data related to this article can be found at https://doi.org/10.1016/j.matchemphys.2021.125616.

References

[1] W. Eerenstein, N.D. Mathur, J.F. Scott, Multiferroic and magnetoelectric materials, Nature 442 (2006) 759–765.

[2] C.M. Leung, J. Li, D. Viehland, X. Zhuang, A review on applications of magnetoelectric composites: from heterostructural uncooled magnetic sensors, energy harvesters to highly efficient power converters, J. Phys. D Appl. Phys. 51 (2018) 263002.

[3] D.N. Astrov, The magnetoelectric effect in antiferromagnetics, Sov. Phys. JETP 11 (1960) 708–709.

[4] G.T. Rado, V.J. Folen, Observation of the magnetically induced magnetoelectric effect and evidence for antiferromagnetic domains, Phys. Rev. Lett. 7 (1961) 310–311.

[5] J.M. Caicedo, J.A. Zapata, M.E. Gómez, P. Prieto, Magnetoelectric coefficient in $BiFeO_3$ compounds, J. Appl. Phys. 103 (2008), 07E306.

[6] P.R. Mickel, H. Jeen, P. Kumar, A. Biswas, A.F. Hebard, Proximate transition temperatures amplify linear magnetoelectric coupling in strain-disordered multiferroic BiMnO$_3$, Phys. Rev. B 93 (2016) 134205.

[7] C.-W. Nan, Magnetoelectric effect in composites of piezoelectric and piezomagnetic phases, Phys. Rev. B 50 (1994) 6082–6088.

[8] R.E. Newnham, D.P. Skinner, L.E. Cross, Connectivity and piezoelectric-pyroelectric composites, Mater. Res. Bull. 13 (1978) 525–536.

[9] T. Ramesh, V. Rajendar, S.R. Murthy, CoFe$_2$O$_4$–BaTiO$_3$ multiferroic composites: role of ferrite and ferroelectric phases on the structural, magneto dielectric properties, J. Mater. Sci. Mater. Electron. 28 (2017) 11779–11788.

[10] J. van den Boomgaard, R.A.J. Born, A sintered magnetoelectric composite material BaTiO$_3$–Ni(Co,Mn)Fe$_2$O$_4$, J. Mater. Sci. 13 (1978) 1538–1548.

[11] R. Gao, Z. Wang, G. Chen, X. Deng, W. Cai, C. Fu, Influence of core size on the multiferroic properties of CoFe$_2$O$_4$@BaTiO$_3$ core shell structured composites, Ceram. Int. 44 (2018) S84–S87.

[12] A. Chaudhuri, K. Mandal, Large magnetoelectric properties in CoFe$_2$O$_4$:BaTiO$_3$ core–shell nanocomposites, J. Magn. Magn. Mater. 377 (2015) 441–445.

[13] R. Liu, Y. Zhao, R. Huang, Y. Zhao, H. Zhou, Multiferroic ferrite/perovskite oxide core/shell nanostructures, J. Mater. Chem. 20 (2010) 10665–10670.

[14] H. Palneedi, V. Annapureddy, S. Priya, J. Ryu, Status and perspectives of multiferroic, magnetoelectric composite materials and applications, Actuators 5 (2016) 9.

[15] C.A.F. Vaz, J. Hoffman, C.H. Ahn, R. Ramesh, Magnetoelectric coupling effects in multiferroic complex oxide composite structures, Adv. Mater. 22 (2010) 2900–2918.

[16] S. Tiwari, S. Vitta, Magnetoelectric and magnetodielectric coupling and microwave resonator characteristics of Ba$_{0.5}$Sr$_{0.5}$Nb$_2$O$_6$/CoCr$_{0.4}$Fe$_{1.6}$O$_4$ multiferroic composite, Sci. Rep. 8 (2018) 11619.

[17] X.M. Chen, Y.H. Tang, I.-W. Chen, Z.C. Xu, S.Y. Wu, Dielectric and magnetoelectric characterization of CoFe$_2$O$_4$/Sr$_{0.5}$Ba$_{0.5}$Nb$_2$O$_6$ composites, J. Appl. Phys. 96 (2004) 6520–6522.

[18] Y.Q. Lin, X.M. Chen, Dielectric relaxations in Sr$_{0.5}$Ba$_{0.5}$Nb$_2$O$_6$/CoFe$_2$O$_4$ high-ε magnetoelectric composite ceramics, Mater. Chem. Phys. 117 (2009) 125–130.

[19] S.R. Jigajeni, S.V. Kulkarni, Y.D. Kolekar, S.B. Kulkarni, P.B. Joshi, Co$_{0.7}$Mg$_{0.3}$Fe$_{2-x}$Mn$_x$O$_4$–Sr$_{0.5}$Ba$_{0.5}$Nb$_2$O$_6$ magnetoelectric composites, J. Alloys Compd. 492 (2010) 405.– 405.

[20] M.M. Sutar, S.R. Kokare, S H Kshirsagar, D.J. Salunkhe, P.B. Joshi, Synthesis and magnetoelectric studies on BSN-CNFM ME composites, AIP Conf. Proc. 1372 (2011) 220–225.

[21] Y.Q. Lin, Y. M Chen, Temperature-stable high dielectric constant and dielectric relaxation in (1-x)Sr$_{0.5}$Ba$_{0.5}$Nb$_2$O$_6$/xNi$_{0.8}$Cu$_{0.2}$Fe$_2$O$_4$ composite ceramics, Ferroelectrics 388 (2009) 153–160.

[22] Y.J. Li, X.M. Chen, R.Z. Hou, Y.H. Tang, Maxwell–wagner characterization of dielectric relaxation in Ni$_{0.8}$Zn$_{0.2}$Fe$_2$O$_4$/Sr$_{0.5}$Ba$_{0.5}$Nb$_2$O$_6$ composite, Solid State Commun. 137 (2006) 120–125.

[23] Y.H. Tang, X.M. Chen, Y.J. Li, X.H. Zheng, Dielectric and magnetoelectric characterization of CoFe$_2$O$_4$/Ba$_{0.55}$Sr$_{0.25}$Ca$_{0.2}$Nb$_2$O$_6$ composites, Mater. Sci. Eng. B 116 (2005) 150–155.

[24] S.R. Jigajeni, A.N. Tarale, D.J. Salunkhe, S.B. Kulkarni, P.B. Joshi, Magnetoelectric and magnetodielectric properties of SBN–CMFO nanocomposites, Appl. Nanosci. 2 (2012) 275–283.

[25] S.S. Rathore, S. Vitta, Large low field room temperature magneto-dielectric response from (Sr$_{0.5}$Ba$_{0.5}$)Nb$_2$O$_6$/Co(Cr$_{0.4}$Fe$_{1.6}$)O$_4$ bulk 3-0 composites, Mater. Sci. Eng. B 204 (2016) 1–7.

[26] J.R.M. Hoyos, E.R. Botero, D. Garcia, R.H.G.A. Kiminami, Simultaneous two-phase formation model in synthesized SBN/NFO using the *in-situ* modified Pechini method, Ceram. Int. 45 (2019) 8593–8599.

[27] C.J. Huang, K. Li, X.Q. Liu, X.L. Zhu, X.M. Chen, Effects of A1/A2-sites occupancy upon ferroelectric transition in (Sr$_x$Ba$_{1-x}$)Nb$_2$O$_6$ tungsten bronze ceramics, J. Am. Ceram. Soc. 97 (2014) 507–512.

[28] R. Köferstein, F. Oehler, S.G. Ebbinghaus, Investigations of nano-crystalline Sr$_{0.5}$Ba$_{0.5}$Nb$_2$O$_6$ and bulk ceramics synthesized by a polymerization method using PEG400, J. Eur. Ceram. Soc. 39 (2019) 1156–1163.

[29] S.S. Rathore, S. Vitta, Enhanced dielectric constant and relaxor behavior realized by dual stage sintering of Sr$_{0.5}$Ba$_{0.5}$Nb$_2$O$_6$, AIP Conf. Proc. 1591 (2014) 133–135.

[30] N.M. Shorrocks, R.W. Whatmore, S.T. Liu, The Electro-elastic and SAW properties of Sr$_{0.5}$Ba$_{0.5}$Nb$_2$O$_6$, J. Phys. D Appl. Phys. 15 (1982) 2469–2481.

[31] R.R. Neurgaonkar, W.K. Cory, Progress in photorefractive tungsten bronze crystals, J. Opt. Soc. Am. B 3 (1986) 274–282.

[32] R. Köferstein, D. Hesse, S.G. Ebbinghaus, Synthesis and characterization of a nano-scaled barium cerate perovskite powder using starch as polymerization agent, Solid State Ionics 203 (2011) 52–56.

[33] S.Q. Ren, L.Q. Wenig, S.-H. Song, F. Li, J.G. Wan, M. Zeng, BaTiO$_3$/CoFe$_2$O$_4$ particulate composites with large high frequency magnetoelectric response, J. Mater. Sci. 40 (2005) 4375–4378.

[34] Program WinXPOW v2.11, Stoe & Cie GmbH, Darmstadt, 2004.

[35] S.D. Norem, M.J. O'Neill, A.P. Gray, The use of magnetic transitions in temperature calibration and performance evaluation of thermogravimetric systems, Thermochim. Acta 1 (1970) 29–38.

[36] M. Breitenbach, H. Deniz, S.G. Ebbinghaus, Magnetoelectric and HR-STEM investigations on eutectic CoFe$_2$O$_4$–Ba$_{1-x}$Sr$_x$TiO$_3$ composites, J. Phys. Chem. Solid. 135 (2019) 109076.

[37] T. Walther, U. Straube, R. Köferstein, S.G. Ebbinghaus, Hysteretic magnetoelectric behavior of CoFe$_2$O$_4$–BaTiO$_3$ composites prepared by reductive sintering and reoxidation, J. Mater. Chem. C 4 (2016) 4792–4799.

[38] V.D. Allred, S.R. Buxton, J.P. McBride, Characteristic properties of thorium oxide particles, J. Phys. Chem. 61 (1957) 117–120.

[39] G.W. Marks, L.A. Monson, Effect of certain group IV oxides on dielectric constant and dissipation factor of barium titanate, Ind. Eng. Chem. 47 (1955) 1611–1620.

[40] R. Köferstein, T. Walther, D. Hesse, S.G. Ebbinghaus, Fine-grained BaTiO$_3$–MgFe$_2$O$_4$ composites prepared by a pechini-like process, J. Alloys Compd. 638 (2015) 141–147.

[41] W. Scharf, H. Weitzel, I. Yaeger, I. Maartense, B.M. Wanklyn, Magnetic structure of CoNb$_2$O$_6$, J. Magn. Magn. Mater. 13 (1979) 121–124.

[42] C.B. Liu, R. Chen, X.Y. Yue, Y.J. Liu, M.M. Shi, H.P. Zhu, C. Domg, Y. Liu, Y.B. Han, J.F. Wang, Z.Z. He, Crystal growth, magnetic property and phase transition of the zigzag-chain antiferromagnet FeNbO$_4$, J. Magn. Magn. Mater. 464 (2018) 108–111.

[43] H. Ehrenberg, G. Wltschek, R. Theissmann, H. Weitzel, H. Fuess, F. Trouw, The magnetic structure of FeNbO$_4$, J. Magn. Magn. Mater. 218 (2000) 261–265.

[44] W. Shen, L. Zhang, B. Zhao, Y. Du, X. Zhou, Growth mechanism of octahedral like nickel ferrite crystals prepared by modified hydrothermal method and morphology dependent magnetic performance, Ceram. Int. 44 (2018) 9809–9815.

[45] E.F. Kneller, F.E. Luborsky, Particle size dependence of coercivity and remanence of single domain particles, J. Appl. Phys. 34 (1963) 656–658.

[46] D.L. Huber, Synthesis, properties, and applications of iron nanoparticles, Small 1 (2005) 485–501.

[47] J.M.D. Coey, Magnetism and Magnetic Materials, Cambridge University Press, Cambridge, 2009.

[48] A. Ghasemi, Compositional dependence of magnetization reversal mechanism, magnetic interaction and Curie temperature of Co$_{1-x}$Sr$_x$Fe$_2$O$_4$ spinel thin film, J. Alloys Compd. 645 (2015) 467–477.

[49] H.M. El-Sayed, A.M. Samy, A.A. Sattar, Infra-red and magnetic studies of Nb-doped Li-ferrites, Phys. Stat. Solid. 201 (2004) 2105–2111.

[50] K.W. Wagner, Erklärung der dielektrischen Nachwirkungsvorgänge auf Grund Maxwellscher Vorstellungen, Arch. Elektrotechnik 2 (1914) 371–387.

[51] A. Sakanas, R. Grigalaitis, J. Banys, L. Mitoseriu, V. Buscaglia, P. Nanni, Broadband dielectric spectroscopy of BaTiO$_3$–Ni$_{0.5}$Zn$_{0.5}$Fe$_2$O$_4$ composite ceramics, J. Alloys Compd. 602 (2014) 241–247.

[52] L.M. Hrib, O.F. Caltun, Effects of the chemical composition of the magnetostrictive phase on the dielectric and magnetoelectric properties of cobalt ferrite–barium titanate composites, J. Alloys Compd. 509 (2011) 6644–6648.

[53] A. Gupta, R. Chatterjee, Dielectric and magnetoelectric properties of BaTiO$_3$–Co$_{0.6}$Zn$_{0.4}$Fe$_{1.7}$Mn$_{0.3}$O$_4$ composite, J. Eur. Ceram. Soc. 33 (2013) 1017–1022.

[54] C.E. Ciomaga, A.M. Neagu, M.V. Pop, M. Airimioaei, S. Tascu, G. Schileo, C. Galassi, L. Mitoseriu, Ferroelectric and dielectric properties of ferrite-ferroelectric ceramic composites, J. Appl. Phys. 113 (2013), 074103.

[55] M.P.K. Sahoo, Z. Yajun, J. Wan, R.N.P. Choudhary, Composition control of magnetoelectric relaxor behavior in multiferroic BaZr$_{0.4}$Ti$_{0.6}$O$_3$/CoFe$_2$O$_4$ composites, J. Alloys. Compd. 657 (2016) 12–20.

[56] C. David, T. Granzow, A. Tunyagi, M. Wöhlecke, Th. Woike, K. Betzler, M. Ulex, M. Imlau, R. Pankrath, Composition dependence of the phase transition temperature in Sr$_x$Ba$_{1-x}$Nb$_2$O$_6$, Phys. Stat. Solid. 201 (2004) R49–R51.

[57] J.S. Kim, S.Y. Cho, M.S. Jang, Ferroelectric and relaxor behavior of Fe-doped Sr$_{0.5}$Ba$_{0.5}$Nb$_{2-x}$Fe$_x$O$_6$ ceramics with a tungsten-bronze structure, J. Kor. Phys. Soc. 51 (2007) 692–696.

[58] S.H. Kshirsagar, A.N. Tarale, S.R. Jigajeni, D.J. Salunkhe, S.B. Kulkarni, P.B. Joshi, Ferroelectric and magnetodielectric properties of cobalt-doped Sr$_x$Ba$_{1-x}$Nb$_2$O$_6$ ceramics, J. Electron. Mater. 44 (2015) 2321–2330.

[59] F. Oehler, H.-T. Langhammer, S.G. Ebbinghaus, Preparation and dielectric properties of CaTaO$_2$N and SrNbO$_2$N ceramics, J. Eur. Ceram. Soc. 37 (2017) 2129–2136.

[60] T. Buttlar, T. Walther, K. Dörr, S.G. Ebbinghaus, Preparation and magnetoelectric behavior of Ni/BaTiO$_3$ heterostructures with 0-3 connectivity, Phys. Status Solidi B (2020) 1900622.

[61] M. Breitenbach, K. Dörr, S.G. Ebbinghaus, Magnetoelectric properties of Co$_{1-x}$Ni$_x$Fe$_2$O$_4$/BaTiO$_3$ heterostructures with 3–3 connectivity obtained by eutectic crystallization, Phys. Status Solidi B (2020) 1900618.

[62] M. Bichurin, V. Petrov, Modeling of Magnetoelectric Effects in Composites, Springer, Dordrecht, 2014, p. 45, et seqq.

[63] A.J. Gualdi, F.L. Zabotto, D. Garcia, A.S. Bhalla, R. Guo, P. Cesar de Camargo, A. J. Aparecido de Oliveira, Dynamic magnetization on the low temperature magnetoelectric effect in multiferroic composites, J. Phys. Condens. Matter 30 (2018) 325803.

[64] M.M. Sutar, S.R. Kokare, S.H. Kshirsagar, D.J. Salunkhe, P.B. Joshi, Synthesis and magnetoelectric studies on BSN-CNFM ME composites, AIP Conf. Proc. 1372 (2011) 220–225.

[65] S.R. Jigajeni, M.M. Sutar, S.M. Salunkhe, P.B. Joshi, Investigation on magnetoelectric and dielectric properties of Co$_{0.9}$Mn$_{0.3}$Fe$_{1.8}$O$_4$–Sr$_{0.5}$Ba$_{0.5}$Nb$_2$O$_6$ composites, J. Mater. Sci. Mater. Electron. 23 (2012) 1678–1687.

[66] T. Volk, D. Isakov, V. Salobutin, L. Ivleva, P. Lykov, V. Ramzaev, M. Wöhlecke, Effects of Ni doping on properties of strontium–barium–niobate crystals, Solid State Commun. 130 (2004) 223–226.

[67] A.A. Ballman, H. Brown, The growth and properties of strontium barium metaniobate, $Sr_{1-x}Ba_xNb_2O_6$, a tungsten bronze ferroelectric, J. Cryst. Growth 1 (1967) 311–314.

[68] B.-M. Jin, R. Guo, A.S. Bhalla, Piezoelectric properties and equivalent circuits of ferroelectric relaxor single crystals, J. Mater. Sci. 32 (1997) 2005–2058.

[69] T.R. Volk, V. Yu. Salobutin, L.I. Ivleva, N.M. Polozkov, R. Pankrath, M. Woehlecke, Ferroelectric properties of strontium barium niobate crystals doped with rare-earth metals, Phys. Solid State 42 (2000) 2129–2136.

[70] J. van Suchtelen, Product properties: a new application of composite materials, Philips Res. Rep. 27 (1972) 28–37.